nature materials

ARTICLES

https://doi.org/10.1038/s41563-020-00816-0

Check for updates

Cation-disordered rocksalt-type high-entropy cathodes for Li-ion batteries

Zhengyan Lun[1,2,8], Bin Ouyang[1,2,8], Deok-Hwang Kwon[1,2], Yang Ha[3], Emily E. Foley[4], Tzu-Yang Huang[5,6], Zijian Cai[1,2], Hyunchul Kim[2], Mahalingam Balasubramanian[7], Yingzhi Sun[1,2], Jianping Huang[2], Yaosen Tian[1,2], Haegyeom Kim[2], Bryan D. McCloskey[5,6], Wanli Yang[3], Raphaële J. Clément[4], Huiwen Ji[6]✉ and Gerbrand Ceder[1,2]✉

High-entropy (HE) ceramics, by analogy with HE metallic alloys, are an emerging class of solid solutions composed of a large number of species. These materials offer the benefit of large compositional flexibility and can be used in a wide variety of applications, including thermoelectrics, catalysts, superionic conductors and battery electrodes. We show here that the HE concept can lead to very substantial improvements in performance in battery cathodes. Among lithium-ion cathodes, cation-disordered rocksalt (DRX)-type materials are an ideal platform within which to design HE materials because of their demonstrated chemical flexibility. By comparing a group of DRX cathodes containing two, four or six transition metal (TM) species, we show that short-range order systematically decreases, whereas energy density and rate capability systematically increase, as more TM cation species are mixed together, despite the total metal content remaining fixed. A DRX cathode with six TM species achieves 307 mAh g^{-1} (955 Wh kg^{-1}) at a low rate (20 mA g^{-1}), and retains more than 170 mAh g^{-1} when cycling at a high rate of 2,000 mA g^{-1}. To facilitate further design in this HE DRX space, we also present a compatibility analysis of 23 different TM ions, and successfully synthesize a phase-pure HE DRX compound containing 12 TM species as a proof of concept.

As an emerging concept in the field of metallic alloys[1,2], high-entropy (HE) materials combine multiple principal elements to create new single-phase materials[3,4]. Over the past few years, the 'HE strategy' has been applied across various fields, including thermoelectricity[5], catalysis[6], superionic conductivity[7] and energy storage[8–10]. The large configurational entropy is believed to enhance the simultaneous solubility of a large number of components, which can then be selected to optimize target properties. In recent studies on the atomic-scale structure of HE compounds, including $(V_{0.2}Nb_{0.2}Ta_{0.2}Mo_{0.2}W_{0.2})C$ (ref. [11]) and $(Mg_{0.2}Co_{0.2}Ni_{0.2}Cu_{0.2}Zn_{0.2})O$ (ref. [12]), a uniform distribution of different transition metals (TMs) was observed, indicating the capability of suppressing cation short-range order (SRO) by mixing together a large number of TM species.

The concept of HE in lithium (Li)-ion electrode materials, if successfully implemented, would be highly attractive as it facilitates the simultaneous optimization of multiple properties. In addition, compositional flexibility would alleviate the industry's reliance on any single critical metal source. The recently developed cation-disordered rocksalt (DRX) cathodes[13–15], in which Li migrates through a percolating network of 0-TM clusters without TM coordination around the activated state, are ideal targets for such HE designs. In DRX cathodes, substantial SRO has been observed, which directly degrades long-range Li transport[16–19]. Monte Carlo simulations[16] have shown that the presence of SRO in DRX cathodes generally leads to reduced Li percolation when compared with that of a random arrangement of metal species. In addition, DRX structures have a large compositional flexibility and can incorporate many TM species[20]. If the HE concept works in DRX cathodes, one would expect that increasing the number of TM species in them would improve Li transport properties by preventing the formation of a single dominant SRO type. Such SRO reduction should result in improved capacity and rate capability.

Here, to evaluate our HE DRX design strategy, three prototype compositions with increasing numbers of TM species are investigated, as shown in Fig. 1a. All three compositions include 30% Li excess (that is, $Li_{1.3}$ per formula unit) to ensure good Li transport without severely compromising the TM redox capacity, and 15% oxygen substituted by fluorine to increase the TM redox reservoir[21–23]. The Mn^{3+}–Ti^{4+} combination[16] was used as baseline, with the $Li_{1.3}Mn^{3+}_{0.4}Ti_{0.3}O_{1.7}F_{0.3}$ composition referred to as TM2 hereafter. Mn^{2+}, Nb^{5+}, Co^{2+} and Cr^{3+} were sequentially incorporated to form $Li_{1.3}Mn^{2+}_{0.2}Mn^{3+}_{0.2}Ti_{0.1}Nb_{0.2}O_{1.7}F_{0.3}$ and $Li_{1.3}Mn^{2+}_{0.1}Co^{2+}_{0.1}Mn^{3+}_{0.1}Cr^{3+}_{0.1}Ti_{0.1}Nb_{0.2}O_{1.7}F_{0.3}$, which contain four and six TM species and are therefore referred to as TM4 and TM6, respectively. We find that although these compounds retain the same long-range order (LRO), the SRO becomes sequentially more suppressed as the number of TM species increases, leading to substantial improvements in energy density and rate capability. This success motivated us to investigate the compatibility of different TM species to facilitate future experimental realizations of high-energy-density HE DRX cathodes. As further proof of the synthetic accessibility of HE DRX compounds, we successfully synthesized a phase-pure DRX composed of twelve TM species in similar concentrations.

[1]Department of Materials Science and Engineering, UC Berkeley, Berkeley, CA, USA. [2]Materials Sciences Division, Lawrence Berkeley National Laboratory, Berkeley, CA, USA. [3]Advanced Light Source, Lawrence Berkeley National Laboratory, Berkeley, CA, USA. [4]Materials Department, UC Santa Barbara, Santa Barbara, CA, USA. [5]Department of Chemical and Biomolecular Engineering, UC Berkeley, Berkeley, CA, USA. [6]Energy Storage and Distributed Resources Division, Lawrence Berkeley National Laboratory, Berkeley, CA, USA. [7]X-ray Science Division, Advanced Photon Source, Argonne National Laboratory, Argonne, IL, USA. [8]These authors contributed equally: Zhengyan Lun, Bin Ouyang. ✉e-mail: huiwenji@lbl.gov; gceder@berkeley.edu

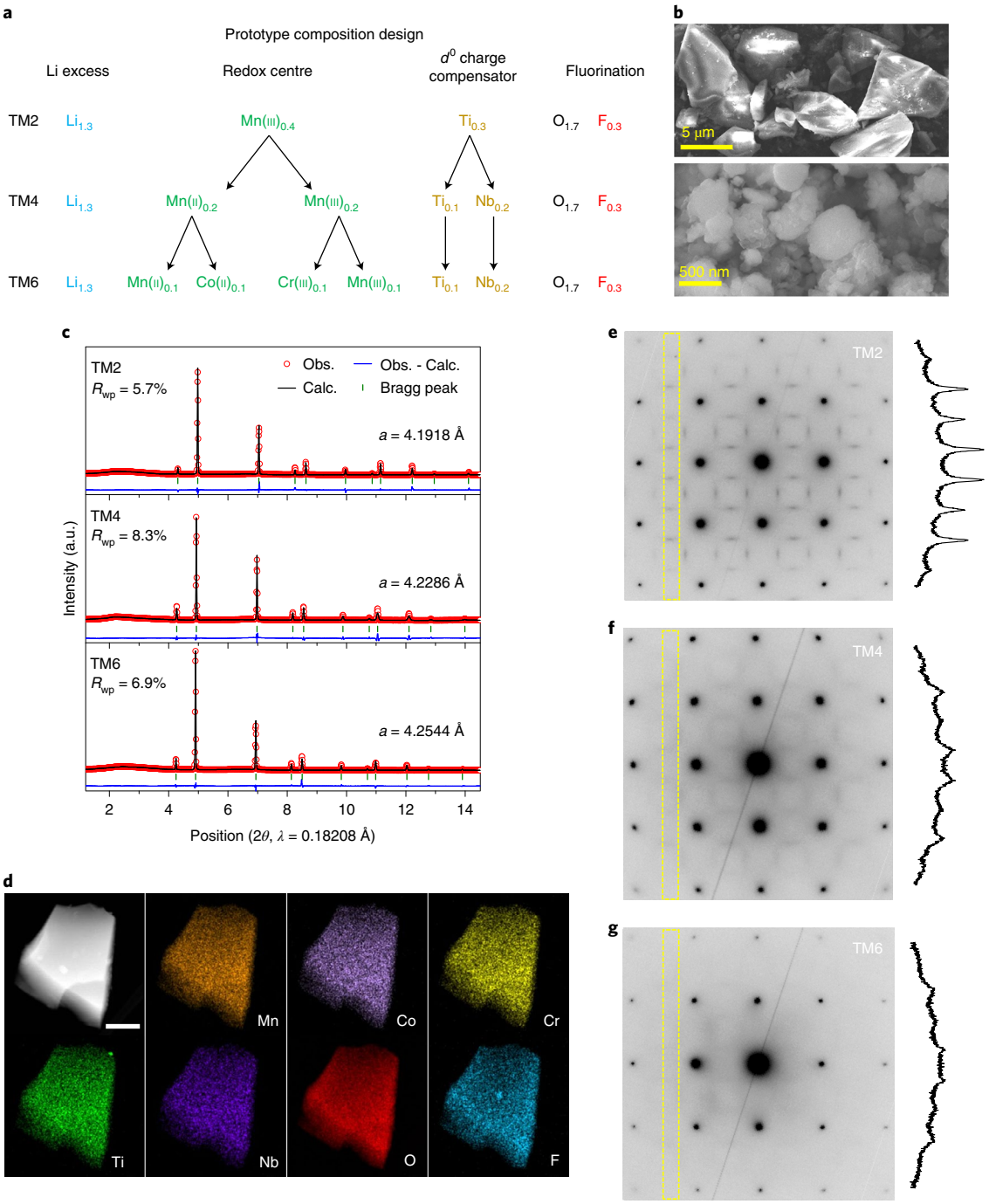

Fig. 1 | Design and structural characterization of the as-synthesized materials. a, Prototype composition design of DRX cathodes with different numbers of TM species. **b**, SEM images of as-synthesized TM6 (top) and TM6 shaker-milled with carbon black (bottom). **c**, Synchrotron XRD patterns and refined lattice constants of the as-synthesized materials at wavelength $\lambda = 0.18208$ Å, where a is the refined lattice constant. R_{wp}, R-factor of the refinement. **d**, STEM/EDS mapping of elemental distribution in a particle cluster of as-synthesized TM6. Scale bar, 300 nm. **e**–**g**, TEM ED patterns collected on as-synthesized TM2 (**e**), TM4 (**f**) and TM6 (**g**) along the [100] zone axis. The round spots, which originate from the LRO in the materials, are indexed to the *Fm*-3*m* space group. The square-like diffuse scattering patterns are attributed to the SRO. The SRO pattern intensity was quantified by integrating the counts within the dashed rectangular regions, and is displayed to the right of the ED patterns.

Structural characterization

All three compounds with different numbers of TM species were successfully synthesized using a traditional solid-state method. Scanning electron microscopy (SEM) analysis reveals that the particle size of the as-synthesized materials reaches approximately 5–10 μm (top panel of Fig. 1b and Supplementary Fig. 1) and can be reduced to 200–500 nm (bottom panel of Fig. 1b and Supplementary Fig. 1) by shaker milling with carbon during electrode fabrication. Synchrotron X-ray diffraction (XRD) patterns (Fig. 1c) and time-of-flight neutron diffraction patterns (Supplementary Fig. 2) confirm the formation of single-phase DRX compounds with no observable impurity peaks. Elemental analysis confirms that the metal ratios in the as-synthesized materials are close to the target compositions, as shown in Supplementary Table 1. Rietveld

refinement yields lattice constants (a) of 4.1918, 4.2286 and 4.2544 Å for TM2, TM4 and TM6, respectively. Scanning transmission electron microscope (STEM)/energy-dispersive spectroscopy (EDS) was applied to investigate the distribution of the multiple elements in the materials. Figure 1d presents the STEM/EDS mapping of a representative particle of the as-synthesized TM6, showing that the different TM species and F are uniformly distributed within the particle. ^{19}F and ^{7}Li solid-state NMR (ssNMR) measurements were further conducted to demonstrate the bulk F incorporation and to detect possible impurities (Supplementary Fig. 3 and Supplementary Note 1).

The cation SRO in the three materials was evaluated using TEM electron diffraction, as shown in Fig. 1e–g. The round Bragg diffraction spots can be indexed to the *Fm*-3*m* space group and originate from the average rocksalt lattice. The square-like diffuse scattering patterns are attributed to SRO[16,24,25]. The intensity of the diffuse scattering, which qualitatively correlates with the strength of the SRO, was integrated within the dashed rectangular regions and compared across the three compounds. The results, displayed to the right of the electron diffraction patterns, clearly indicate that increasing the number of TM species from two to six suppresses the SRO in the DRX structures, as evidenced by the reduced intensity of the SRO pattern in the electron diffraction patterns. The experimental observation of the reduction in SRO from TM2 to TM6 is further corroborated computationally, as presented in Supplementary Fig. 6 and Supplementary Note 3.

Electrochemical performance

The electrochemical performance of the three materials was evaluated using galvanostatic cycling. When cycled between 1.5 and 4.7 V at a rate of 20 mA g^{-1}, TM2 delivers a capacity (specific energy) of 220 mAh g^{-1} (704 Wh kg^{-1}), as shown in Fig. 2a. With more TM species in the DRX structure, TM4 delivers 269 mAh g^{-1} (849 Wh kg^{-1}) (Fig. 2b), which further increases to 307 mAh g^{-1} (955 Wh kg^{-1}) for TM6 (Fig. 2c). An extensive set of other compositions containing subsets of the six TMs in the TM6 were synthesized and characterized (shown in Supplementary Fig. 5 and Supplementary Note 2), corroborating the overall trend that a larger number of TM species, rather than the incorporation of any specific TM, leads to a higher capacity. Galvanostatic intermittent titration measurements (shown in Supplementary Fig. 4a) were also performed, indicating that the polarization is greatly reduced as the number of TM species in the DRX structure increases. The results support our design strategy of reducing SRO to improve Li transport, increase capacity and reduce polarization.

The benefits of increasing the TM variety are further corroborated by rate performance tests on the three materials, as shown in Fig. 2d–f. For TM2, the discharge capacity decreases from 220 mAh g^{-1} when cycled at 20 mA g^{-1} to 58 mAh g^{-1} at 2,000 mA g^{-1}, corresponding to a 74% capacity loss at the high rate. For a similar rate increase, the capacity loss is reduced to 58% for TM4 and to 45% for TM6. The rate capability of the TM6 compound is remarkable, with a discharge capacity of more than 170 mAh g^{-1} delivered at the very high cycling rate of 2,000 mA g^{-1}, corresponding to a 7 min (dis)charge process.

Redox mechanism

The redox behaviour in the three materials was elucidated by combining hard X-ray absorption spectroscopy to capture the TM electronic states, and soft X-ray resonant inelastic X-ray scattering (RIXS) for the oxygen state. The TM redox behaviour in TM6 was studied using in situ hard X-ray absorption spectroscopy, with experimental details provided in the Methods. The X-ray near-edge structure spectra of the pristine, top-of-charge and end-of-discharge states at the Cr, Mn and Co K-edge X-ray absorption spectra (XAS) are presented in Fig. 3a–c, respectively. Representative oxide references are also shown to facilitate the data interpretation. The oxidation states of Cr are estimated from the pre-edge intensity[26], and those of Mn and Co are estimated from the energy of the rising edge[27]. It can be estimated from Fig. 3a that approximately 70% of Cr^{3+} is oxidized to Cr^{6+} at the top of charge, which contributes ~65 mAh g^{-1} of capacity. As observed in Fig. 3b, the Mn K edge shifts to a higher energy and approaches that of MnO_2 (Mn^{4+}) when charged to 4.7 V. Full oxidation of Mn should contribute ~90 mAh g^{-1} of capacity. The Co K edge only shifts close to that of the Co_3O_4 reference at the top-of-charge state, which suggests the oxidation of Co^{2+} to approximately $Co^{8/3+}$, equivalent to an ~20 mAh g^{-1} capacity contribution. Following discharge, all three metal K edges shift back to their initial energy positions, indicating good reversibility of the metal redox. The Co^{2+}/Co^{3+} and Cr^{3+}/Cr^{6+} redox processes are both only partially utilized, along with the full utilization of the Mn^{2+}/Mn^{4+} redox, leading to approximately 175 mAh g^{-1} of the overall capacity being contributed by the TM redox during the first cycle. Results and analysis of the TM redox behaviour at other states of charge are presented in Supplementary Figs. 7 and 8 and Supplementary Note 4.

A TM redox capacity that is much smaller than the observed reversible capacity suggests the participation of oxygen redox, which is a phenomenon that often arises in Li-rich cathode materials[28,29]. We therefore performed high-efficiency mapping of O K-edge RIXS to detect any changes of the oxygen electronic states. Previous studies have established that O K-edge RIXS mapping can circumvent the limitation of conventional O K-edge XAS and therefore serves as the tool-of-choice for detecting lattice oxygen redox[30]. In particular, a feature that appears at an excitation energy of ~531 eV and emission energy of ~524 eV is found to be a fingerprint of oxidized oxygen in a range of battery electrodes[30,31]. Indeed, a comparison of the O K-edge RIXS maps from pristine and top-of-charge TM6 (Fig. 3d,e) clearly reveals the characteristic oxidized oxygen feature at 4.7 V (red arrow in Fig. 3e), indicating some oxygen oxidation on charge. RIXS cuts at the characteristic 531 eV excitation energy at three states of charge (pristine, charged and discharged) during the first cycle are provided in Fig. 3f. The strong feature of oxidized oxygen (dashed line) appears at 4.7 V and disappears when fully discharged, indicating reversible oxygen oxidation and reduction processes.

The redox mechanisms in TM2 and TM4 were studied by similar methods (Supplementary Figs. 10–12 and Supplementary Note 5), confirming that Mn is mostly oxidized to Mn^{4+} in both materials, contributing approximately 140 mAh g^{-1} (TM2) and 180 mAh g^{-1} (TM4) to the overall capacity. The remainder of the capacity in both materials is provided by oxygen redox, as suggested by O K-edge RIXS results (Supplementary Fig. 11). These observations indicate that there is no substantial difference in the redox behaviour of the three materials, further confirming that an increased theoretical TM redox capacity is not the main reason for the improved capacities when increasing the number of TM species from TM2 to TM4 or TM6.

TM compatibility in HE DRXs

Given that DRX materials have generally suffered from low rate capability[15,16], the high rates that can be achieved with the TM6 compound are remarkable. The rate capability and capacity in DRX materials seems to be largely connected to the percolation of 0-TM channels, the connection of tetrahedral units on which no TM is present[15,16]. For fully random cation systems, percolation theory predicts 0-TM percolation to be prevalent for the 0.3Li excess used in our compounds, whereas SRO (that is, deviations from the random state) has been shown to reduce percolation in a very substantial way[16,19,32]. In particular, SRO of the γ–$LiFeO_2$-type that exhibits a preference for tetrahedral units with two Li and two TM are electrostatically favoured but have a destructive effect on 0-TM

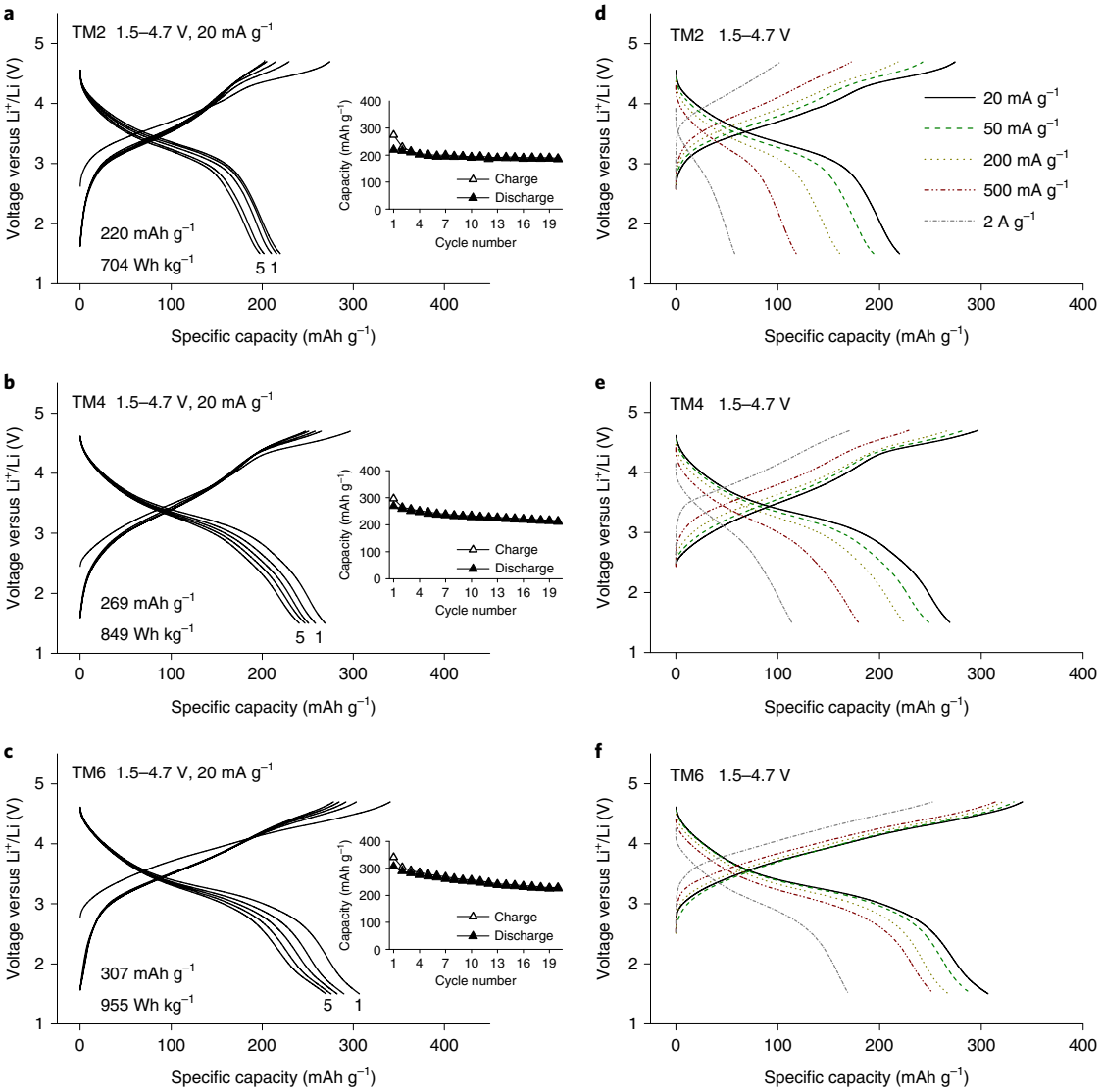

Fig. 2 | Electrochemical performance of the three compounds. a–c, Voltage profiles of TM2 (**a**), TM4 (**b**) and TM6 (**c**) within the voltage window of 1.5–4.7 V at 20 mA g^{-1} and room temperature. The corresponding capacity retention plots are shown as insets. **d–f**, Rate capability of TM2 (**d**), TM4 (**e**) and TM6 (**f**) showing the first-cycle voltage profiles of all three compounds when cycled between 1.5 and 4.7 V at 20, 50, 200, 500 and 2,000 mA g^{-1}. The legend in **d** also applies to **e** and **f**.

percolation[14]. The prevalence of this SRO type is remarkable given γ–$LiFeO_2$-type LRO is not that common[33]. This may be because in long-ranged ordered structures, elastic energy contributions originating from the size difference of the ions are very important, and often select the α–$NaFeO_2$-type layered structure[34]. Without such long-range interactions, γ–$LiFeO_2$-type SRO becomes prevalent in the disordered state, leading to degradation of Li transport[14]. For this reason, the ability to reduce or eliminate cation SRO is an important design insight. Our strategy to minimize SRO by the use of many different TM species, all in similar concentrations, was inspired by the recent observations of nearly random cation distribution in several metal and oxide HE compounds[11,12]. As our work shows, this strategy also works in DRX oxides: by increasing the number of TM species, the intensity of SRO is substantially reduced, as evidenced by the TEM electron diffraction results shown in Fig. 1e–g. Consistent with our understanding of percolation theory, this then also improves capacity and rate performance (Fig. 2).

To understand how broad the opportunity space is of possible HE DRX compounds, we use ab initio methods to evaluate which metals and valence states may coexist in a DRX compound. We approached this by estimating the mixing temperature of potential DRX compounds from the calculated energy difference between a structure with pseudo-random cations and the competing phases in the convex hull, as described in the Methods. The mixing temperature is considered a qualitative measure of the synthetic accessibility, with a lower mixing temperature indicating better synthesizability, as it requires less thermal energy to mix the metal ions. We considered 23 cations: Mn^{2+}, Fe^{2+}, Co^{2+}, Ni^{2+}, Mg^{2+}, Zn^{2+}, Cr^{3+}, V^{3+}, Mn^{3+}, Fe^{3+}, Co^{3+}, Ni^{3+}, Ga^{3+}, Al^{3+}, Ti^{4+}, Zr^{4+}, Mn^{4+}, V^{4+}, Sn^{4+}, Mo^{4+}, Nb^{5+}, V^{5+} and Sb^{5+}. All possible combinations of these elements that fall into our five prototype compositions ($Li_{1.3}$ and $F_{0.3}$ per formula unit, see Methods) were considered, yielding 7,965 distinct compounds. Compounds containing two or three TM species are defined as low-entropy DRX (LE DRX), whereas those with at least four TM species are defined as HE DRX. The resulting probability distribution of the mixing temperature is plotted in Fig. 4a. In addition, the boxplots in the top panel show the most likely range of mixing temperature for both LE and HE DRX materials. Given the approximations

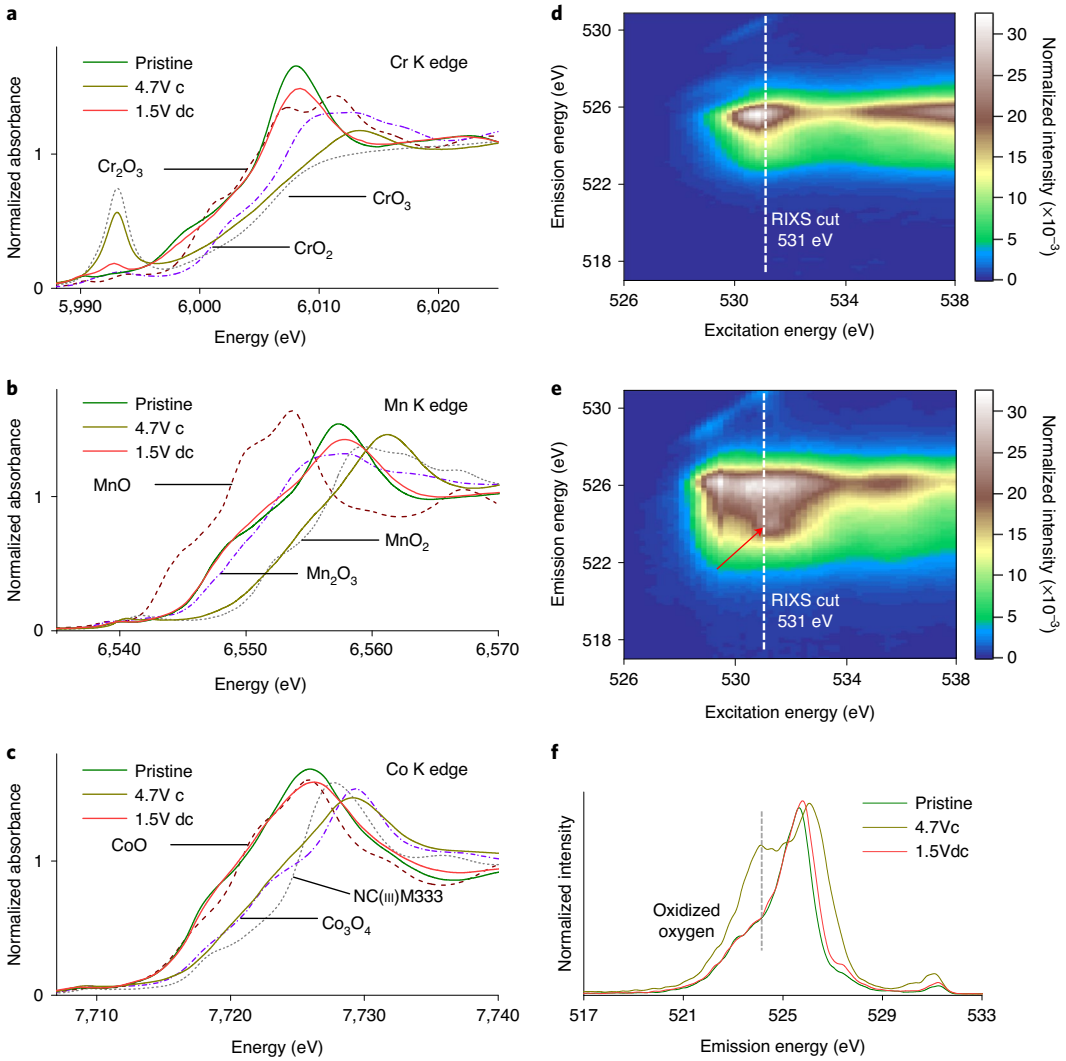

Fig. 3 | Redox mechanism of TM6. a–c, X-ray near-edge structure spectra in pristine, top-of-charge (4.7 V c) and end-of-discharge (1.5 V dc) states from the first cycle at the Cr K edge (**a**), Mn K edge (**b**) and Co K edge (**c**) acquired from operando XAS measurements. **d**,**e**, O K-edge RIXS map of TM6 in pristine (**d**) and top-of-charge (**e**) states (4.7 V). The red arrow marks the oxidized oxygen feature. **f**, O K-edge RIXS spectra collected at an excitation energy of 531 eV (marked by the dashed lines in **d** and **e**) in pristine, top-of-charge (4.7 V c) and end-of-discharge (1.5 V dc) states from the first cycle. The dashed line marks the oxidized oxygen feature.

(density functional theory (DFT), quasi-random structure for the random state and an approximate entropy model), this temperature should not be taken as quantitative, but we expect qualitative differences between compound groups to be well represented. The approximate mixing temperatures of HE DRX compounds are generally more than 500 K lower than those of LE DRX compounds. In other words, when synthesized at the same temperature, HE DRXs will be structurally more random.

Our dataset also enables us to identify chemistries that are particularly well suited to creating accessible low-SRO DRX compounds. The periodic table in Fig. 4b shows (with a colour scale) the median mixing temperature of the systems that contain the given element. In the LE DRX, Ti and Mo enhance disorder, consistent with their presence in many DRX compositions[15,20]. For HE DRX, there is considerably less chemical variation of the mixing temperature, consistent with the idea that it is the extra entropy from the high number of elements that lowers the mixing temperature, rather than chemical specificity. This can be clearly observed for elements such as Mg^{2+}, Cr^{3+} and Sb^{5+}, which can form secondary phases in LE DRXs but are more likely to be incorporated in HE DRXs.

In Fig. 4c, we compare the redox compatibility and chemical compatibility of TM ion pairs. Cation pairs that are not redox-compatible (that is, they were found to transfer charge between them when present together) are greyed out. For example, when Mn^{3+} and V^{3+} coexist in a DRX compound, charge transfer occurs, oxidizing V^{3+} to V^{5+} while reducing Mn^{3+} to Mn^{2+}, which is consistent with a previous finding that V^{4+}/V^{5+} oxidation occurs before Mn^{2+}/Mn^{3+} oxidation upon charge in a Mn^{2+}–V^{4+}-based DRX cathode[35]. The full map of charge-transfer and potential redox reactions between various TM pairs is presented in Supplementary Fig. 18. The chemical compatibility is quantified by the median mixing temperature of the compounds that contain both elements. The compatibility of different TM pairs is shown on a normalized scale between 0 (highly compatible) and 1 (not compatible) in Fig. 4c. The scale is derived from the mixing temperatures as $(T - T_{min})/(T_{max} - T_{min})$, in which T_{max} and T_{min} are the maximum and minimum mixing temperatures among all of the TM pairs. All of the redox-active species demonstrate good chemical compatibility when redox compatibility is satisfied, except Cr^{3+}. Species such as Mg^{2+}, Zn^{2+}, Ga^{3+}, Al^{3+} and Sn^{4+} are less compatible with the other TMs and their concentrations should be kept

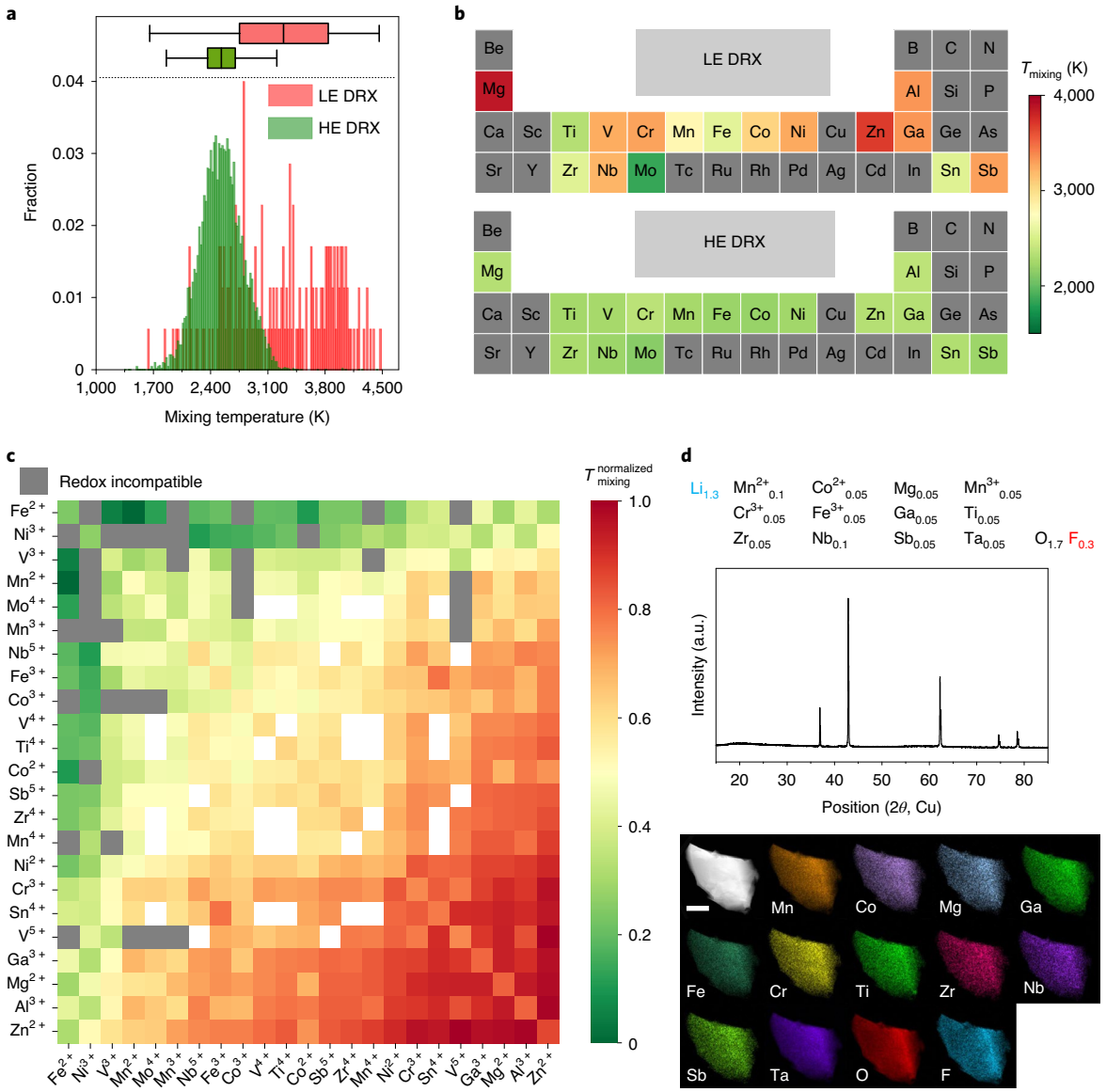

Fig. 4 | Compatibility of metals in HE DRX cathodes. a, Probability distribution of mixing temperature for LE and HE DRX cathodes. The box plot (top) shows the median and interquartile range of mixing temperatures for LE and HE DRXs. **b**, Periodic table-type heat map of mixing temperatures of different elements in LE and HE DRXs. The elements shaded grey were not included in the calculations. **c**, Normalized mixing temperature different TM species in DRX compounds. The colour bar indicates increasing incompatibility from green to red. See the text for details of the normalized quantity plotted. Grey fields are redox incompatible couples. White squares are TM couples that were not included in our compositions. **d**, Demonstration of a HE DRX containing 12 TM species (TM12). The XRD pattern (top) confirms the phase purity and the STEM/EDS mapping (bottom) shows the uniform distribution of different elements. Scale bar, 400 nm.

low. Following these guidelines, a HE DRX compound containing 12 TM species each at similar concentration was designed (Fig. 4d) and successfully prepared using a traditional solid-state method. The XRD pattern (middle panel of Fig. 4d) confirms the phase purity without observable impurities, and the STEM/EDS mapping (lower panel of Fig. 4d) also indicates a homogeneous distribution of all of the elements. We note that although it shows reasonable capacity (Supplementary Fig. 14), the TM12 compound is not optimized for electrochemical performance but demonstrates that DRX materials containing such a high number of TM components can be synthesized.

Although mixing a large number of TM ions can serve as a general strategy to suppress SRO and improve Li transport in DRXs, sufficient TM redox capacity needs to be maintained to achieve good electrochemical performance. There can be a trade-off between high entropy and high energy density because incorporating more TM species would dilute the concentration of each TM, especially the redox-active TM species. Thus, the mixing of various redox-active TM species is a good strategy to frustrate SRO without diluting the TM redox capacity. The incorporation of double-redox centres, such as Mn^{2+} (Mn^{2+}/Mn^{4+}), V^{3+} (V^{3+}/V^{5+}) and Mo^{4+} (Mo^{4+}/Mo^{6+}) is especially beneficial because they provide high electron capacities and are compatible with each other in their low oxidation states. Cr^{3+} offers a three-electron redox (Cr^{3+}/Cr^{6+}) with a high voltage, however, it tends to form competing layered phases, which limits the solubility of Cr^{3+} in a DRX compound (Supplementary Note 6). Note that because of their overlap with oxygen oxidation, Fe^{2+}, Co^{2+} and Ni^{2+} are regarded as one-electron redox centres in DRXs

as demonstrated in previous studies[36,37], although their oxidation to a +4 state may be achieved in other structures[27,38]. High-valency d^0 TM species, such as Ti^{4+} and Nb^{5+}, demonstrate low mixing temperatures and are highly compatible with most of the redox-active TM species, and thus can be used as charge compensators to further increase the TM redox capacity.

Several practical issues are worth noting regarding the potential engineering and commercialization of HE DRX cathodes. DRX cathodes often exhibit larger voltage hysteresis (Supplementary Fig. 4b) than conventional layered ones, such as Li-stoichiometric NMC (Ni, Co, Mn) oxides, the precise origin of which is so far unclear. Furthermore, although the bulk DRX lattice remains intact and robust upon cycling (Supplementary Fig. 15), which may further be enhanced by the entropy-stabilization effect[12] in HE DRXs, cathode–electrolyte interfacial reactions (Supplementary Fig. 16) might still occur and result in capacity degradation upon cycling. For example, TM6 shows slightly lower capacity retention (around 76% retained after 20 cycles) than that of TM2 (84% after 20 cycles) and TM4 (80% after 20 cycles). This can presumably be attributed to the larger degree of cathode–electrolyte interfacial side-reactions in TM6, as indicated by a higher amount of CO_2 evolution observed in the differential electrochemical mass spectrometer (DEMS) tests (Supplementary Figs. 12 and 13).

Outlook for HE DRX cathodes

The concept of HE compounds has become increasingly important in materials science because of its wide applicability to various fields and its ability to enlarge the design space for functional materials. The outstanding chemical flexibility of the DRX compounds makes them an ideal platform to exercise this opportunity and create cathode materials that combine high energy density and high rate capability. As demonstrated in this work, the cathode compound composed of six different TM species achieves a capacity of $>300\,mAh\,g^{-1}$ with an energy density of $>950\,Wh\,kg^{-1}$ at $20\,mA\,g^{-1}$, which is approximately 40% larger than the capacity of the low-entropy TM2 compound. In addition, the incorporation of a large number of TM species reduces the extent of SRO in the DRX lattice and dramatically improves Li transport. TM6 exhibits excellent rate capability, retaining a discharge capacity of $>170\,mAh\,g^{-1}$ when cycled at a very high rate of $2\,A\,g^{-1}$. This allows a complete (dis)charge within 7 min, with a gravimetric capacity delivered comparable to that of $LiCoO_2$.

We believe that the combination of the chemical flexibility of DRX materials and the ability to improve Li transport by creating more random configurations with a high number of metal components, as demonstrated in this paper, creates a potentially vast space of interesting new cathode compounds. To navigate this space, our thermodynamic analyses of the compatibility between various TM pairs reveal two important guidelines (that is, redox compatibility and chemical compatibility) when designing HE DRX cathodes. From the perspective of compositional design, a Li excess level of 1.2–1.3 per formula unit is typically suggested, which is expected to provide a reasonable amount of percolating Li without greatly limiting the TM redox capacity. Fluorination can be applied to further increase the TM redox reservoir, which is beneficial for cycle life. When mixing many species to suppress the unfavourable SRO, prioritizing the use of redox-active TMs is preferred for a large TM capacity. TM ions capable of multi-electron redox and with good chemical compatibility, such as Mn^{2+} and V^{3+}, are highly preferred, whereas a small amount of the less-soluble Cr^{3+} is also beneficial for its high-voltage three-electron redox process. Fe^{2+} (to provide Fe^{2+}/Fe^{3+} redox capacity) may also be a good redox centre, with a low mixing temperature and high natural abundance. For non-redox-active species, high-valence metal ions, such as Ti^{4+} and Nb^{5+}, could be used as charge compensators to enable a larger TM redox reservoir. Other factors, such as the concentration of each TM component within a fixed HE chemical space, or even the synthesis condition (Supplementary Fig. 20 and Supplementary Note 7) are also expected to affect the configurational entropy, the degree of SRO and thus the electrochemical performance. Further exploration of advanced HE DRX cathodes is likely to lead to even more improved cathode materials. We would also call for investigations of the capacity fading mechanism in DRX cathodes, such as the effect of electrolyte breakdown at the high voltage cutoff typically used for DRX materials. New electrolyte strategies or surface protection are expected to enhance the cycle life of the HE DRX cathodes. In addition, optimization of the rate capability, as presented in this work and other studies[39] may allow for larger particle sizes to be used, which would reduce surface reactivity.

Online content

Any methods, additional references, Nature Research reporting summaries, source data, extended data, supplementary information, acknowledgements, peer review information; details of author contributions and competing interests; and statements of data and code availability are available at https://doi.org/10.1038/s41563-020-00816-0.

Received: 6 April 2020; Accepted: 1 September 2020;
Published online: 12 October 2020

References

1. Cantor, B., Chang, I. T. H., Knight, P. & Vincent, A. J. B. Microstructural development in equiatomic multicomponent alloys. *Mater. Sci. Eng. A* **375-377**, 213–218 (2004).
2. Yeh, J. W. et al. Nanostructured high-entropy alloys with multiple principal elements: novel alloy design concepts and outcomes. *Adv. Eng. Mater.* **6**, 299–303 (2004).
3. Zhang, R.-Z. & Reece, M. J. Review of high entropy ceramics: design, synthesis, structure and properties. *J. Mater. Chem. A* **7**, 22148–22162 (2019).
4. Oses, C., Toher, C. & Curtarolo, S. High-entropy ceramics. *Nat. Rev. Mater.* **5**, 295–309 (2020).
5. Zhang, R.-Z., Gucci, F., Zhu, H., Chen, K. & Reece, M. J. Data-driven design of ecofriendly thermoelectric high-entropy sulfides. *Inorg. Chem.* **57**, 13027–13033 (2018).
6. Batchelor, T. A. A. et al. High-entropy alloys as a discovery platform for electrocatalysis. *Joule* **3**, 834–845 (2019).
7. Bérardan, D., Franger, S., Meena, A. & Dragoe, N. Room temperature lithium superionic conductivity in high entropy oxides. *J. Mater. Chem. A* **4**, 9536–9541 (2016).
8. Wang, Q. et al. Multi-anionic and-cationic compounds: new high entropy materials for advanced Li-ion batteries. *Energy Environ. Sci.* **12**, 2433–2442 (2019).
9. Sarkar, A. et al. High entropy oxides for reversible energy storage. *Nat. Commun.* **9**, 3400 (2018).
10. Zhao, C., Ding, F., Lu, Y., Chen, L. & Hu, Y.-S. High-entropy layered oxide cathodes for Na-ion batteries. *Angew. Chem. Int. Ed.* **59**, 264–269 (2020).
11. Harrington, T. J. et al. Phase stability and mechanical properties of novel high entropy transition metal carbides. *Acta Mater.* **166**, 271–280 (2019).
12. Rost, C. M. et al. Entropy-stabilized oxides. *Nat. Commun.* **6**, 8485 (2015).
13. Lee, J. et al. Unlocking the potential of cation-disordered oxides for rechargeable lithium batteries. *Science* **343**, 519–522 (2014).
14. Urban, A., Lee, J. & Ceder, G. The configurational space of rocksalt-type oxides for high-capacity lithium battery electrodes. *Adv. Energy Mater.* **4**, 1400478 (2014).
15. Clément, R. J., Lun, Z. & Ceder, G. Cation-disordered rocksalt transition metal oxides and oxyfluorides for high energy lithium-ion cathodes. *Energy Environ. Sci.* **13**, 345–373 (2020).
16. Ji, H. et al. Hidden structural and chemical order controls lithium transport in cation-disordered oxides for rechargeable batteries. *Nat. Commun.* **10**, 592 (2019).
17. Lun, Z. et al. Design principles for high-capacity Mn-based cation-disordered rocksalt cathodes. *Chem* **6**, 153–168 (2020).
18. Clément, R. J., Kitchaev, D., Lee, J. & Gerbrand, C. Short-range order and unusual modes of nickel redox in a fluorine-substituted disordered rocksalt oxide lithium-ion cathode. *Chem. Mater.* **30**, 6945–6956 (2018).
19. Ouyang, B. et al. Effect of fluorination on lithium transport and short-range order in disordered-rocksalt-type lithium-ion battery cathodes. *Adv. Energy Mater.* **10**, 1903240 (2020).

20. Urban, A., Abdellahi, A., Dacek, S., Artrith, N. & Ceder, G. Electronic-structure origin of cation disorder in transition-metal oxides. *Phys. Rev. Lett.* **119**, 176402 (2017).
21. Chen, R. et al. Disordered lithium-rich oxyfluoride as a stable host for enhanced Li^+ intercalation storage. *Adv. Energy Mater.* **5**, 1401814 (2015).
22. Lee, J. et al. Reversible Mn^{2+}/Mn^{4+} double redox in lithium-excess cathode materials. *Nature* **556**, 185–190 (2018).
23. Lun, Z. et al. Improved cycling performance of Li-excess cation-disordered cathode materials upon fluorine substitution. *Adv. Energy Mater.* **9**, 1802959 (2019).
24. De Ridder, R., van Tendeloo, G. & Amelinckx, S. A cluster model for the transition from the short-range order to the long-range order state in f.c.c. based binary systems and its study by means of electron diffraction. *Acta Crystallogr. Sect. A* **32**, 216–224 (1976).
25. Hata, S., Matsumura, S., Kuwano, N. & Oki, K. Short range order and its transformation to long range order in Ni_4Mo. *Acta Materialia* **46**, 881–892 (1998).
26. Balasubramanian, M., McBreen, J., Davidson, I., Whitfield, P. & Kargina, I. In situ X-ray absorption study of a layered manganese-chromium oxide-based cathode material. *J. Electrochem. Soc.* **149**, A176–A184 (2002).
27. Yoon, W.-S. et al. Investigation of the charge compensation mechanism on the electrochemically Li-ion deintercalated $Li_{1-x}Co_{1/3}Ni_{1/3}Mn_{1/3}O_2$ electrode system by combination of soft and hard X-ray absorption spectroscopy. *J. Am. Chem. Soc.* **127**, 17479–17487 (2005).
28. Luo, K. et al. Charge-compensation in 3*d*-transition-metal-oxide intercalation cathodes through the generation of localized electron holes on oxygen. *Nat. Chem.* **8**, 684–691 (2016).
29. Seo, D.-H. et al. The structural and chemical origin of the oxygen redox activity in layered and cation-disordered Li-excess cathode materials. *Nat. Chem.* **8**, 692–697 (2016).
30. Yang, W. & Devereaux, T. P. Anionic and cationic redox and interfaces in batteries: advances from soft X-ray absorption spectroscopy to resonant inelastic scattering. *J. Power Sources* **389**, 188–197 (2018).
31. Dai, K. et al. High reversibility of lattice oxygen redox quantified by direct bulk probes of both anionic and cationic redox reactions. *Joule* **3**, 518–541 (2019).
32. Jones, M. A. et al. Short-range ordering in a battery electrode, the 'cation-disordered' rocksalt $Li_{1.25}Nb_{0.25}Mn_{0.5}O_2$. *Chem. Commun.* **55**, 9027–9030 (2019).
33. Hewston, T. A. & Chamberland, B. L. A survey of first-row ternary oxides $LiMO_2$ (M = Sc-Cu). *J. Phys. Chem. Solids* **48**, 97–108 (1987).
34. Wu, E. J., Tepesch, P. D. & Ceder, G. Size and charge effects on the structural stability of $LiMO_2$ (M= transition metal) compounds. *Phil. Mag. B* **77**, 1039–1047 (1998).
35. Kitchaev, D. A. et al. Design principles for high transition metal capacity in disordered rocksalt Li-ion cathodes. *Energy Environ. Sci.* **11**, 2159–2171 (2018).
36. Lee, J. et al. A new class of high capacity cation-disordered oxides for rechargeable lithium batteries: Li–Ni–Ti–Mo oxides. *Energy Environ. Sci.* **8**, 3255–3265 (2015).
37. Yabuuchi, N. et al. Origin of stabilization and destabilization in solid-state redox reaction of oxide ions for lithium-ion batteries. *Nat. Commun.* **7**, 13814 (2016).
38. Yabuuchi, N. et al. P2-type $Na_x[Fe_{1/2}Mn_{1/2}]O_2$ made from earth-abundant elements for rechargeable Na batteries. *Nat. Mater.* **11**, 512–517 (2012).
39. Ji, H. et al. Ultrahigh power and energy density in partially ordered lithium-ion cathode materials. *Nat. Energy* **5**, 213–221 (2020).

Methods

Synthesis. All of the DRX oxyfluoride compounds were synthesized using a traditional solid-state method. Li_2CO_3 (Alfa Aesar, ACS, 99% min), MnO (Stream Chemicals Inc., 99%), $CoCO_3$ (Alfa Aesar, 99.5%), Mn_2O_3 (Alfa Aesar, 99.9%), Cr_2O_3 (Sigma-Aldrich, 98%), TiO_2 (Alfa Aesar, 99.9%), Nb_2O_5 (Sigma-Aldrich, 99.99%) and LiF (Alfa Aesar, 99.99%) were used as precursors. For TM12, additional precursors of Fe_2O_3 (Aldrich, nanopowder), Ga_2O_3 (Alfa Aesar, 99.999%), $Zr(OH)_4$ (Aldrich, 97%), Sb_2O_5 (Alfa Aesar, 99.998%), Ta_2O_5 (Aldrich, 99.99%) and MgF_2 (Sigma-Aldrich, 99.9%) were used. All of the precursors were stoichiometrically mixed in ethanol (except around 10% more Li_2CO_3 and 5% more $CoCO_3$ were added to compensate for possible loss during synthesis) with a Retsch PM 400 planetary ball mill at a rate of 180 r.p.m. for 12 h. The precursors were then dried in an oven at 70 °C overnight and pelletized. The precursor pellets were pre-eated at 600 °C for 3 h followed by sintering at 1,000 °C under an argon atmosphere, except for TM2, MCN and MCT, which were sintered at 1,050 °C. The duration of sintering was 6 h. The pellets were then fast cooled in an argon atmosphere, transferred to a glovebox and ground into powders.

Electrochemistry. All of the cathode films were composed of the active materials, Super C65 (Timcal) and polytetrafluoroethylene (PTFE, DuPont, Teflon 8A) at a weight ratio of 70:20:10. To make the cathode films, 280 mg of the as-synthesized active materials and 80 mg of Super C65 were mixed and shaker-milled for 90 min in an argon atmosphere using an SPEX 800M mixer/mill, and PTFE was later added and manually mixed with the shaker-milled mixture for 40 min. The components were then rolled into thin films inside a glovebox. Commercial 1 M $LiPF_6$ in an ethylene carbonate and dimethyl carbonate solution (1:1 volume ratio) was used as the electrolyte. A glass microfibre filter (Whatman) was used as the separator. FMC Li metal foil was used as the anode. Coin cells were assembled inside the glovebox and tested on an Arbin battery test instrument at room temperature. The loading density of the films was approximately 3–4 mg cm^{-2} based on the active materials. For the rate-capability tests, a smaller loading density of approximately 2.5 mg cm^{-2} based on the active materials was used. The specific capacities were calculated on the basis of the weight of active materials (70%) in the cathode films. For the galvanostatic intermittent titration measurements, each step in the voltage profiles corresponds to a galvanostatic charge/discharge of 10 mAh g^{-1} at a rate of 20 mA $^{-1}$ followed by a 6 h relaxation step.

Characterization. Synchrotron XRD patterns of the as-synthesized compounds were obtained at Beamline 28-ID-2 at Brookhaven National Lab. Lab XRD patterns were obtained using a Rigaku Miniflex 600 or a Bruker D8 ADVANCE diffractometer (Cu source) in the 2θ range of 15–85°. Rietveld refinement was performed using PANalytical X'pert HighScore Plus software[40]. Elemental analysis was performed using direct current plasma emission spectroscopy (PerkinElmer Optima 5300 DV Optical Emission Spectrometer) for lithium, titanium, chromium, manganese, cobalt and niobium. The fluorine content was measured using a Cole-Parmer PB-2750414 fluoride ion-selective electrode. SEM images were collected using a Zeiss Gemini Ultra-55 analytical field-emission SEM at the Molecular Foundry at Lawrence Berkeley National Lab (LBNL). STEM/EDS/electron diffraction measurements were performed on a JEM-2010F and Titan X microscopes at the Molecular Foundry at LBNL. To compare the intensity of electron diffraction patterns, the same acquisition time was used and all of the particles examined were similar in size. Neutron powder diffraction analysis was performed using the Nanoscale Ordered Materials Diffractometer (NOMAD) at the Spallation Neutron Source at Oak Ridge National Laboratory. The samples for the neutron diffraction experiment were prepared using ^{7}Li-enriched precursors (^7LiF and $^7Li_2CO_3$). The refinement was performed using TOPAS software[41].

ssNMR spectroscopy. ssNMR data were collected on the TM2, TM4 and TM6 pristine powders using a Bruker Avance 300 MHz (7.05 T) wide-bore NMR spectrometer with Larmor frequencies of 282.40 and 116.64 MHz at room temperature. The data were obtained at 60 kHz magic-angle spinning using a 1.3-mm double-resonance HX probe. ^{19}F and ^{7}Li NMR data were referenced against lithium fluoride (LiF, $\delta(^{19}F) = -204$ ppm and $\delta(^7Li) = -1$ ppm). Lineshape analysis was performed using the Bruker Topspin software and SOLA lineshape simulation package[42].

The resonant frequency range of ^{19}F nuclei in TM2, TM4 and TM6 was larger than the excitation bandwidth of the radiofrequency pulse used in the NMR experiment. To obtain the full spectrum, 11 spin echo spectra were collected for TM2 and 9 spin echo spectra were collected for TM4 and TM6. These spectra were obtained using frequency steps of 140 ppm (739.5 kHz) from −759 to 361 ppm, where the step size was slightly lower than the excitation bandwidth of the radiofrequency pulse. Individual sub-spectra were processed using a zero-order phase correction and then added to give an overall sum spectrum in absorption mode that required no further phase correction. This method—termed frequency stepping[43,44], spin echo mapping[45] or variable offset sumulative spectrum[46]—uniformly excites the broad ^{19}F signals by providing a large excitation bandwidth. Individual ^{19}F spin echo spectra were collected using a 90° radiofrequency pulse of 5.2 µs and a 180° radiofrequency pulse of 10.4 µs at 100 W, with a recycle delay of 30 ms. For reference, a spin echo spectrum was collected on LiF using similar radiofrequency pulses but with a recycle delay of 30 s. A ^{19}F spectrum obtained on the empty probe using acquisition parameters similar to those used for the ^{19}F spectra collected on the DRX samples showed no substantial background signal.

^{7}Li spin echo spectra of all of the samples were obtained using a 90° radiofrequency pulse of 0.7 µs and a 180° radiofrequency pulse of 1.4 µs at 100 W. A recycle delay of 30 s was used for LiF, and a recycle delay of 0.5 s was used for all of the DRX samples. Additional spin echo spectra were acquired with a recycle delay of 3 s for TM4 and TM6 to capture the entire ^{7}Li diamagnetic signal for quantification purposes; this was unnecessary for TM2, as ^{7}Li spin lattice relaxation was much faster for this compound.

Ex situ and operando hard XAS. XAS spectra were acquired in transmission mode at beamline 20-BM-B at the Advanced Photon Source. The incident beam energy was selected using a Si (111) monochromator. The energy calibration was performed by simultaneously measuring the spectra of an appropriate metal foil. Harmonic rejection was accomplished using a Rh-coated mirror. All of the ex situ samples were electrode films composed of active materials, Super C65 and PTFE in a weight ratio of 70:20:10, and the loading density (based on the active materials) was determined using Hephaestus software[47]. They were assembled as coin cells, charged to the designated capacities, and then disassembled and washed with DMC in a glovebox (except for the pristine materials). Additional spectra of reference standards were also measured to facilitate interpretation. Operando hard XAS spectra of TM6 at the Cr, Mn and Co K-edges were measured using a modified coin-cell setup within the voltage window of 1.5–4.7 V at a cycling rate of 16 mA g^{-1}. The cell was held at the top of charge for 30 min before discharging. The loading density (based on the active material) was approximately 10 mg cm^{-3}. The raw data were processed (normalization and energy calibration) using Athena software[47].

RIXS. O K-edge RIXS maps were obtained at beamline 8.0.1 at the iRIXS endstation at the Advanced Light Source. The cathode samples were mounted on a 1-inch copper sample holder and transferred from an argon glovebox into the ultrahigh vacuum main chamber using a sealed sample transfer kit. The beam slit size was set to 40/40, and the samples were continuously moved within a small region relative to the focused beam position to minimize photo damage. The photon energy was calibrated using the first peak of the standard TiO_2 as 531 eV. The emission spectra at each excitation energy were collected for 90 s. The RIXS map was generated from the emission spectra at different excitation energies using an Igor code written by the Yang group[48]. The emission energy was calibrated based on the elastic peak line on the RIXS map. Key samples such as the pristine, fully charged and fully discharged were measured multiple times, each with fresh sample preparation.

DEMS measurement. The custom-built DEMS instrument, cell geometry and instrument operation are described in previous publications[49–51]. The electrochemical cells used with the DEMS device were prepared in a glovebox using a modified Swagelok design, and the cathode film was composed of the active materials, carbon black and PTFE in a weight ratio of 70:20:10, with a loading density of ~10 mg cm^{-2} (based on the active materials). The electrolyte, separators and anodes used were identical to those used for the coin-cell tests in this study. The assembled cells were charged at 20 mA g^{-1} (except for the multi-cycle test, which used a rate of C/10) under a static head of positive argon pressure (approximately 1.2 bar) at room temperature after being appropriately attached to the DEMS instrument. The accumulated gas in the cell was purged by 500 µl of pulsed argon gas every 10 min. The swept-out gas was subsequently sent into mass-spectrometer chamber for analysis. Calibration of the mass spectrometry at various partial pressure of O_2, CO_2 or H_2 in argon was conducted for quantification. CO evolution was estimated by the method described in a previous publication[52]. Mass-spectrometer signals of POF_3 fragments ($m/z = 104$ and $m/z = 85$) were used to monitor POF_3 release.

DFT calculations. First-principles DFT calculations were performed to obtain an accurate description of the structural energies and oxidation states of the different cathode materials. All of the calculations were performed using the projector-augmented wave (PAW) method[53] as implemented in the Vienna Ab initio Simulation Package (VASP)[54]. A rotationally averaged Hubbard U correction[55,56] was used to correct the self-interaction error in oxides containing Co, Cr, Fe, Mn, Mo, Ni and V. The U parameters were obtained from a previously reported calibration to oxide formation energies[56]. For all of the calculations, a reciprocal space discretization of 25 k-points per Å^{-1} was applied, and the convergence criteria were set as 10^{-6} eV for electronic loops and 0.02 eV Å^{-1} for ionic loops.

Special quasi-random structure and mixing temperature calculation. Special quasi-random structures (SQSs) are periodic structures whose atomic distributions are selected such that the cluster correlations approach the expected value in a random atomic arrangement as closely as possible for a given structure size[57]. Given this feature, SQSs are an appropriate choice for investigating the properties of rocksalt materials with full disorder. In the alloy

community, for example, SQSs have been successfully used to evaluate mixing enthalpies[58] and to model the electronic structure of random alloys[59]. Our previous studies on DRXs using SQSs also indicate that these structures can be effective tools for quantifying the phase stability[60], electronic structure[20] and voltage curves[61,62]. To model the random cation distribution of the fully disordered rocksalt materials, we generated SQSs for all three prototype compositions: $Li_{1.3}(M_a)^{3+}_{0.4}(M_b)^{4+}_{0.3}O_{1.7}F_{0.3}$, $Li_{1.3}(M_a)^{2+}_{0.2}(M_b)^{3+}_{0.2}(M_c)^{4+}_{0.1}(M_c)^{5+}_{0.2}O_{1.7}F_{0.3}$ and $Li_{1.3}(M_a)^{2+}_{0.1}(M_b)^{2+}_{0.1}(M_c)^{3+}_{0.1}(M_d)^{3+}_{0.1}(M_e)^{4+}_{0.1}(M_f)^{5+}_{0.2}O_{1.7}F_{0.3}$, as well as two additional compositions containing three TMs and five TMs, respectively: $Li_{1.3}(M_a)^{2+}_{0.3}(M_b)^{3+}_{0.1}(M_c)^{5+}_{0.3}O_{1.7}F_{0.3}$ and $Li_{1.3}(M_a)^{2+}_{0.1}(M_b)^{2+}_{0.1}(M_c)^{3+}_{0.2}(M_d)^{4+}_{0.1}(M_e)^{5+}_{0.2}O_{1.7}F_{0.3}$. With the energetics calculated from DFT, the mixing temperatures of DRX materials were estimated using the equation

$$T_{\mathrm{mixing}} = \frac{E_{\mathrm{hull}}}{k_{\mathrm{B}}\left(0.65ln0.65 + 0.15ln0.15 + 0.85ln0.85 + \sum_M x_M lnx_M\right)}.$$

E_{hull} is the energy above the convex hull per cation in the phase diagram constructed with all phases in the relevant chemical space available in an internal database containing phases from the ICSD as well as some compounds generated using data-mined substitution rules[63]. The variable x_M refers to the atomic fraction of metal per cation site and k_B is the Boltzmann constant. The DRXs with only two or three TMs are grouped into LE DRXs, whereas those containing more than three TMs are classified as HE DRXs. The mixing temperature of a specific DRX composition is calculated as its energy above the convex hull divided by the maximum configurational entropy it gains upon disordering. A complete list of all competing phases generated by our phase diagram analysis is provided in Supplementary Table 2.

Cluster expansion, Monte Carlo simulation, SRO and percolation analysis. A cluster expansion model has been constructed to describe the energetics of the complete configurational space of Li^+–Mn^{2+}–Co^{2+}–Mn^{3+}–Cr^{3+}–Ti^{4+}–Nb^{5+}–O^{2-}–F^-. In such a cluster expansion, the configurational energy dependence is captured by an expansion into different cluster functions, which can be formulated as[64,65]:

$$E = \sum_{i,\mathrm{sp1}} J_i^{\mathrm{sp1}}\sigma_i^{\mathrm{sp1}} + \sum_{i,j,\mathrm{sp1,sp2}} J_{ij}^{\mathrm{sp1sp2}}\sigma_i^{\mathrm{sp1}}\sigma_j^{\mathrm{sp2}} + \sum_{i,j,k,\mathrm{sp1,sp2,sp3}} J_{ijk}^{\mathrm{sp1sp2sp3}}\sigma_i^{\mathrm{sp1}}\sigma_j^{\mathrm{sp2}}\sigma_k^{\mathrm{sp3}} \ldots \ldots$$

Here, σ_i^{sp} corresponds to the occupancy of certain site(s) i, j, k with a certain species sp and J refers to the effective cluster interactions.

In HE DRX materials, a cation site can be occupied by Li and six other types of metals while the anion sites can be occupied by either O^{2-} or F^-. For each system, pair interactions up to 7.1 Å, triplet interactions up to 4.0 Å and quadruplet interactions up to 4.0 Å based on a rocksalt lattice with $a = 3.0$ Å were included in the cluster expansion formulism. The effective cluster interactions were fitted to DFT energies of sampled structures using a L1-regularized least-squares regression approach[66], with the regularization parameters selected to minimize cross-validation error[17,19,35,66–68]. The DFT results of 6,154 structures are applied to fit the cluster expansion, which end up with a cluster expansion model that has root-mean-squared error of 7.62 meV per atom.

With the constructed cluster expansion, we then perform Monte Carlo simulation at 1,273 K for three experimental compositions (TM2, TM4 and TM6). For each composition, percolation analysis[14,19] and Warren–Cowley SRO parameter[69] calculations are performed on 10,000 Monte Carlo structures.

Data availability

All relevant data within the article are available from the corresponding authors on reasonable request. Source data are provided with this paper.

References

40. Degen, T., Sadki, M., Bron, E., König, U. & Nénert, G. The HighScore suite. *Powder Diffrac.* **29**, S13–S18 (2014).
41. Coelho, A. *Topas Academic* version 4.1 (Coelho Software, 2007).
42. *TopSpin Academic* version 3.6.2 (Bruker Software, 2019).
43. O'Dell, L. A., Rossini, A. J. & Schurko, R. W. Acquisition of ultra-wideline NMR spectra from quadrupolar nuclei by frequency stepped WURST–QCPMG. *Chem. Phys. Lett.* **468**, 330–335 (2009).
44. Pell, A. J., Clément, R. J., Grey, C. P., Emsley, L. & Pintacuda, G. Frequency-stepped acquisition in nuclear magnetic resonance spectroscopy under magic angle spinning. *J. Chem. Phys.* **138**, 114201 (2013).
45. Sananes, M., Tuel, A., Hutchings, G. & Volta, J. Characterization of different precursors and activated vanadium phosphate catalysts by ^{31}P NMR spin echo mapping. *J. Catal.* **148**, 395–398 (1994).
46. Massiot, D. et al. ^{71}Ga and ^{69}Ga nuclear magnetic resonance study of β-Ga_2O_3: resolution of four-and six-fold coordinated Ga sites in static conditions. *Solid State Nucl. Magn. Reson.* **4**, 241–248 (1995).
47. Ravel, B. & Newville, M. ATHENA, ARTEMIS, HEPHAESTUS: data analysis for X-ray absorption spectroscopy using IFEFFIT. *J. Synchrotron Radiat.* **12**, 537–541 (2005).
48. Wu, J. et al. Elemental-sensitive detection of the chemistry in batteries through soft X-ray absorption spectroscopy and resonant inelastic X-ray scattering. *J. Visual. Exp.* **134**, e57415 (2018).
49. McCloskey, B. D., Bethune, D., Shelby, R., Girishkumar, G. & Luntz, A. Solvents' critical role in nonaqueous lithium–oxygen battery electrochemistry. *J. Phys. Chem. Lett.* **2**, 1161–1166 (2011).
50. McCloskey, B. D. et al. On the efficacy of electrocatalysis in nonaqueous Li–O_2 batteries. *J. Am. Chem. Soc.* **133**, 18038–18041 (2011).
51. McCloskey, B. D. et al. Twin problems of interfacial carbonate formation in nonaqueous Li–O_2 batteries. *J. Phys. Chem. Lett.* **3**, 997–1001 (2012).
52. Renfrew, S. E. & McCloskey, B. D. Residual lithium carbonate predominantly accounts for first cycle CO_2 and CO outgassing of Li-stoichiometric and Li-rich layered transition-metal oxides. *J. Am. Chem. Soc.* **139**, 17853–17860 (2017).
53. Kresse, G. & Joubert, D. From ultrasoft pseudopotentials to the projector augmented-wave method. *Phys. Rev. B* **59**, 1758–1775 (1999).
54. Kresse, G. & Furthmüller, J. Efficiency of ab-initio total energy calculations for metals and semiconductors using a plane-wave basis set. *Comput. Mater. Sci.* **6**, 15–50 (1996).
55. Dudarev, S. L., Botton, G. A., Savrasov, S. Y., Humphreys, C. J. & Sutton, A. P. Electron-energy-loss spectra and the structural stability of nickel oxide: an LSDA+U study. *Phys. Rev. B* **57**, 1505–1509 (1998).
56. Wang, L., Maxisch, T. & Ceder, G. Oxidation energies of transition metal oxides within the GGA+U framework. *Phys. Rev. B* **73**, 195107 (2006).
57. Zunger, A., Wei, S. H., Ferreira, L. G. & Bernard, J. E. Special quasirandom structures. *Phys. Rev. Lett.* **65**, 353–356 (1990).
58. Shin, D., van de Walle, A., Wang, Y. & Liu, Z.-K. First-principles study of ternary fcc solution phases from special quasirandom structures. *Phys. Rev. B* **76**, 144204 (2007).
59. Wei, S. H., Ferreira, L. G., Bernard, J. E. & Zunger, A. Electronic properties of random alloys: special quasirandom structures. *Phys. Rev. B* **42**, 9622–9649 (1990).
60. Urban, A., Matts, I., Abdellahi, A. & Ceder, G. Computational design and preparation of cation-disordered oxides for high-energy-density Li-ion batteries. *Adv. Energy Mater.* **6**, 1600488 (2016).
61. Abdellahi, A., Urban, A., Dacek, S. & Ceder, G. The effect of cation disorder on the average Li intercalation voltage of transition-metal oxides. *Chem. Mater.* **28**, 3659–3665 (2016).
62. Abdellahi, A., Urban, A., Dacek, S. & Ceder, G. Understanding the effect of cation disorder on the voltage profile of lithium transition-metal oxides. *Chem. Mater.* **28**, 5373–5383 (2016).
63. Hautier, G., Fischer, C., Ehrlacher, V., Jain, A. & Ceder, G. Data mined ionic substitutions for the discovery of new compounds. *Inorg. Chem.* **50**, 656–663 (2011).
64. Sanchez, J. M., Ducastelle, F. & Gratias, D. Generalized cluster description of multicomponent systems. *Phys. A* **128**, 334–350 (1984).
65. Wolverton, C. & de Fontaine, D. Cluster expansions of alloy energetics in ternary intermetallics. *Phys. Rev. B* **49**, 8627–8642 (1994).
66. Nelson, L. J., Hart, G. L. W., Zhou, F. & Ozoliņš, V. Compressive sensing as a paradigm for building physics models. *Phys. Rev. B* **87**, 035125 (2013).
67. Richards, W. D., Dacek, S. T., Kitchaev, D. A. & Ceder, G. Fluorination of lithium-excess transition metal oxide cathode materials. *Adv. Energy Mater.* **8**, 1701533 (2018).
68. Ji, H. et al. Computational investigation and experimental realization of disordered high-capacity Li-ion cathodes based on Ni redox. *Chem. Mater.* **31**, 2431–2442 (2019).
69. Cowley, J. M. X-Ray measurement of order in single crystals of Cu_3Au. *J. Appl. Phys.* **21**, 24–30 (1950).

Acknowledgements

This work was supported by Umicore Specialty Oxides and Chemicals, the Assistant Secretary for Energy Efficiency and Renewable Energy, Vehicle Technologies Office of the US Department of Energy (DOE) under contract no. DEAC02-05CH11231, under the Advanced Battery Materials Research (BMR) Program. Work at the Molecular Foundry was supported by the Office of Science and Office of Basic Energy Sciences of the US DOE under contract no. DE-AC02-05CH11231. The NMR experimental work reported here made use of the shared facilities of the UCSB MRSEC (NSF DMR 1720256), a member of the Material Research Facilities Network. This research used resources at the Spallation Neutron Source, a DOE Office of Science User Facility operated by the Oak Ridge National Laboratory. This research used resources from beamline 28-ID of the National Synchrotron Light Source II, a US DOE Office of Science User Facility operated for the DOE Office of Science by Brookhaven National Laboratory under contract no. DE-SC0012704. Work at the Advanced Light Source is supported by the US DOE Office of Science User Facility under contract no. DE-AC02-05CH11231. This research used resources of the Advanced Photon Source, an Office of Science User Facility operated for the US DOE Office of Science by Argonne National Laboratory,

and was supported by the US DOE under contract no. DE-AC02-06CH11357. The computational analysis was performed using computational resources sponsored by the US DOE Office of Energy Efficiency and Renewable Energy and located at the National Renewable Energy Laboratory, and computational resources were provided by Extreme Science and Engineering Discovery Environment (XSEDE), which was supported by National Science Foundation grant no. ACI1053575, as well as the National Energy Research Scientific Computing Center (NERSC), a DOE Office of Science User Facility supported by the Office of Science and the US DOE under contract no. DE-AC02-05CH11231. The authors thank J. Liu for help with the neutron diffraction measurements.

Author contributions

Z.L. planned the project with H. J. and G.C. Z.L. designed, synthesized, characterized (XRD) and electrochemically tested the proposed compounds with the help from Z.C., J.H., Haegyeom Kim and H.J. B.O. performed DFT, SQS calculations, cluster expansion and Monto Carlo simulations and analysed the data. D.-H.K. acquired and analysed TEM data. Y.H. acquired and analysed the RIXS data with W.Y. E.E.F. acquired and analysed the NMR data with R.J.C. T.-Y.H. acquired and analysed DEMS data with input from B.D.M. Z.L. acquired and analysed the XAS data with the help from Hyunchul Kim, M.B., Z.C. and Y.S. Y.T. performed the SEM. The manuscript was written by Z.L. and revised by B.O., R.J.C., H.J. and G.C. with the help of all other authors. All authors contributed to discussions.

Competing interests

The authors declare no competing interests.

Additional information

Supplementary information is available for this paper at https://doi.org/10.1038/s41563-020-00816-0.

Correspondence and requests for materials should be addressed to H.J. or G.C.

Reprints and permissions information is available at www.nature.com/reprints.